Journal of Alloys and Compounds 696 (2017) 1067–1079

Contents lists available at ScienceDirect

Journal of Alloys and Compounds

journal homepage: http://www.elsevier.com/locate/jalcom

Dynamic mechanical response and microstructural evolution of extruded Mg AZ31B plate over a wide range of strain rates

Weigui Zhang [a, *], Yicong Ye [b], Liangju He [c], Peijie Li [a], Husheng Zhang [d, **]

[a] Department of Mechanical Engineering, Tsinghua University, Beijing 100084, China
[b] College of Aerospace and Materials Engineering, National University of Defense Technology, Changsha 410073, China
[c] School of Aerospace Engineering, Tsinghua University, Beijing 100084, China
[d] State Key Laboratory of Nonlinear Mechanics, Institute of Mechanics, Chinese Academy of Sciences, Beijing 100190, China

ARTICLE INFO

Article history:
Received 14 September 2016
Received in revised form
1 December 2016
Accepted 3 December 2016
Available online 5 December 2016

Keywords:
Extruded AZ31B plate
Gradient texture
Dynamic mechanical behavior
Deformation mechanism
Microstructural evolution

ABSTRACT

In this research, the mechanical behaviors of extruded AZ31B Mg plate along normal direction (ND) were investigated over a wide range of strain rates. High strain rate tests were carried out using a split Hopkinson pressure bar at room temperature. The corresponding deformation mechanisms, texture evolution and microstructure changes were analyzed by utilizing optical microscope (OM), X-ray diffraction (XRD), electron backscatter diffraction (EBSD) and transmission electron microscopy (TEM). It is found that the mechanical responses exhibit both sigmoidal hardening and power-law hardening behaviors under compression at high strain rate ranges of 1068–5647 s^{-1}. The prismatic type textures of the skin layer and center layer of the AZ31B plate determine its mechanical behaviors. The sigmoidal hardening behaviors are resulted from the formation and development of {10-12} extension twinning at the initial stage of deformation. Whereas the power-law hardening behaviors are resulted from non-basal ⟨c+a⟩ dislocation slip dominated the deformation at the initial deformation stage. Experimental results indicate the critical resolved shear stress (CRSS) for extension twinning and non-basal ⟨c+a⟩ dislocation slip are insensitive to strain rate, but the latter CRSS is significantly higher than the former CRSS. The flow stress is insensitive to strain rate if plastic deformation is dominated by extension twinning, while it increases with the increase of strain rate if plastic deformation is dominated by non-basal ⟨c+a⟩ dislocation slip. Dynamic recrystallization (DRX) took place if the AZ31B plate was compressed at strain ranges of 4737–5647 s^{-1}, resulting in a decrease in flow stress and a significant increase in ductility.

1. Introduction

Magnesium (Mg) alloys are increasingly used in design and manufacture of automobile, light armored vehicle and spacecraft component due to their low weight and high specific strength [1–5]. In these applications, Mg alloys are often challenged by instantaneous high strain rate loading environment. Study on the mechanical properties of materials under high strain rate loading is of great significance for both materials science and structural design. In the case of structural design, components need to meet the requirements over a wide range of loading rates. Thus it is necessary to understand the mechanical behavior of the material in response to different strain rates. In the case of material science, mechanical properties of material under different strain rates reflect not only the macromechanical behaviors, but also its microscopic properties. Study on the relationship between material's microstructure and its dynamic mechanical property not only demonstrates academic importance for understanding the deformation mechanisms of material over a wide range of loading rates, but provides significant guidance for design and preparation of materials suitable for fierce dynamic loading conditions as well.

The mechanisms that govern the deformation of Mg alloys at quasi-static or low strain rate (<10 s^{-1}) have been extensively studied in the past decades [6–15]. In general, slip and twinning are the predominant deformation mechanisms in Mg alloys. The dominant slip systems are (0001)⟨11-20⟩ basal slip system, (10-10)⟨11-20⟩ prismatic slip system and (11-22)⟨11-2-3⟩ pyramidal slip

* Corresponding author.
** Corresponding author.
E-mail addresses: CASC529@163.com (W. Zhang), hshang@lnm.imech.ac.cn (H. Zhang).

http://dx.doi.org/10.1016/j.jallcom.2016.12.041
0925-8388/

system [9–11]. The basal and prismatic slip systems have the ⟨a⟩ type Burger's vector, they are not able to accommodate general plastic deformations along *c*-axis. The pyramidal slip system has Burger's vector containing both ⟨c⟩ and ⟨a⟩ components, so it can accommodate plastic deformations along *c*-axis. The activation of a specific slip system is dependent on the deformation temperature and the crystallographic texture. Twinning plays an important role in the deformation of Mg alloys as well. The usually observed twinning modes in Mg alloys are {10-12}⟨10-11⟩ extension twinning and {10-11}⟨10-12⟩ contraction twinning. Additionally, {10-11}-{10-12} secondary twinning could also take place under certain conditions [14]. The extension twinning supplies extension along *c*-axis, whereas the contraction twinning and secondary twinning supply contraction along *c*-axis. As pointed out by previous studies [7,15], the net contributions of both contraction twinning and secondary twinning to the total deformation is not significant. It is now widely accepted that the pyramidal ⟨c+a⟩ slip accommodates most of the compression along *c*-axis.

The CRSS value is the key factor in determining the operation of slip or twinning mechanism. It is generally accepted that the order of CRSS for both slip and twinning mechanisms are: $CRSS_{basal} < CRSS_{extension\ twinning} < CRSS_{prismatic} < CRSS_{pyramidal} < CRSS_{contraction\ twinning}$ [10]. Thus basal ⟨a⟩ slip and {10–12} extension twinning are most easily activated mechanisms during deformation. In fact, the CRSS for above deformation mechanisms are highly influenced by temperature. Although the CRSS for basal slip and extension twinning are temperature independent, the CRSS for prismatic slip and pyramidal slip decrease with the increase of temperature. Thus the activity of these non-basal slip systems will increase at high temperature. Additionally, for Mg alloys, at temperature higher than 200 °C, DRX occurs simultaneously [16,17]. Therefore, high temperature will activate additional mechanisms, resulting in an increase in ductility and a decrease in flow stress.

The deformation of Mg alloys is highly dependent on texture and orientation of *c*-axis relative to loading direction. If *c*-axis is mainly subjected to tension, {10–12} extension twinning predominates at the early stage of deformation, followed by rapid strain hardening at the subsequent stage due to interactions of dislocation-dislocation and dislocation-twin [10,11]. If *c*-axis is mainly subjected to compression, non-basal slip and {10-11} contraction twinning are active at the initial stage of deformation, resulting in higher flow stress and relative lower strain hardening [18]. The operations of different deformation mechanisms give rise to an asymmetry in the mechanical properties. Recently, the mechanical behaviors of Mg alloys at high strain rates (~10^3 s^{-1}) and their corresponding deformation mechanisms have been investigated by many researchers [19–28]. An excellent work was completed by Uiacia and co-workers [20], who investigated the dynamic (~10^3 s^{-1}) mechanical behavior and deformation mechanism of AZ31 Mg alloy sheet at room and high temperature. Their results reveal that extension twinning is enhanced at high strain rates and is the predominant deformation mechanism at the first stage of deformation at both room and high temperature. Furthermore, at high strain rates a remarkable tension/compression asymmetry is observed even at high temperature due to the operation of different deformation mechanisms. Dudamell et al. [22] systematically investigated the microstructural evolution of an AZ31 sheet during high strain rate (~10^3 s^{-1}) deformation by electron backscatter diffraction and neutron diffraction. It has been found that formation of extension twins are enhanced dramatically at high strain rates, but contraction and secondary twinning are barely influenced by stain rate. In addition, dislocation accumulation and rearrangement occurs during deformation, which is responsible for the formation of geometrically necessary boundaries as well as higher strain hardening. Prasad et al. [26] reviewed the dynamic behaviors of polycrystalline pure Mg and two Mg alloys, AZ31B and ZK60. It is found that crystallographic texture, grain size, and alloying elements have significant influence on the dynamic deformation behaviors. The flow stress is insensitive to strain rate if deformation is dominated by extension twinning. Whereas some strain rate dependent flow stress is observed if deformation is dominated by dislocation mechanisms. Dixit et al. [27] studied the microstructural evolution and deformation mechanisms in pure Mg under high strain rate (~10^3 s^{-1}) compression by using EBSD and TEM. If dynamically compressed along extrusion direction (compression axis is perpendicular to the *c*-axis), a large number of extension twins form at the initial deformation stage, then ⟨c+a⟩ dislocation slip take place in the twin region to accommodate the subsequent plastic deformation. Experimental results demonstrate that both extension twinning and dislocation activity are needed to accommodate deformation under high strain rate loading.

Extruded or rolled Mg alloys thick plate (>10 mm) are usually utilized as protective armors for light vehicles and light aircraft. And in the practical situation, the actual impact direction of projectile is mostly along the ND of plate. Additionally, for the thick plate, there are variations in the microstructure and texture along ND. The textures along ND generally have a gradient distribution and the microstructure is non-uniform. Considering this practical situation, the aim of this work is to investigate the mechanical response of extruded AZ31B Mg alloy plate along ND under high strain rate (~10^3 s^{-1}) conditions using a split Hopkinson pressure bar. Detailed microstructure and texture examination by OM, XRD, EBSD and TEM have been carried out in deformed samples in order to elucidate the predominant deformation mechanisms and microstructural evolution.

2. Experimental procedure

2.1. Materials

In this work, the extruded AZ31B Mg plate with initial thickness of 10 mm was selected for study. Chemical compositions of the AZ31B alloys measured by X-ray fluorescence spectrometer (XRF) are presented in Table 1. The initial microstructure and textures of the AZ31B alloy are shown in Fig. 1. As shown in Fig. 1 (a), the microstructure is composed of two kinds of grains, the large grains elongate along extrusion direction (ED) and the small equiaxied grains distribute among the large elongated grains. The small equiaxied grains suggest that they have fully recrystallized during hot extrusion, whereas the large elongated grains remain in the worked state. Orientation distribution function (ODF) was used to exactly characterize the initial textures of skin layer and center layer of the AZ31B plate. The measurement of texture and calculation of ODF will be described later. Given the symmetry of hexagonal structure, ODF section with $\varphi_2 = 0°$, 30° were used to characterize the textures of material. Textures of skin layer and center layer of AZ31B plate are shown in Fig. 1 (b, c), which indicate the textures are prismatic type and the main component is {11-20}⟨10-10⟩, in which the *c*-axis is tilted away from the ND toward the transverse direction (TD).

Table 1
The chemical compositions detected by XRF of extruded AZ31B Mg alloy (wt. %).

Sample	Mg	Al	Zn	Mn	Other
AZ31B	95.576	3.362	0.750	0.296	0.016

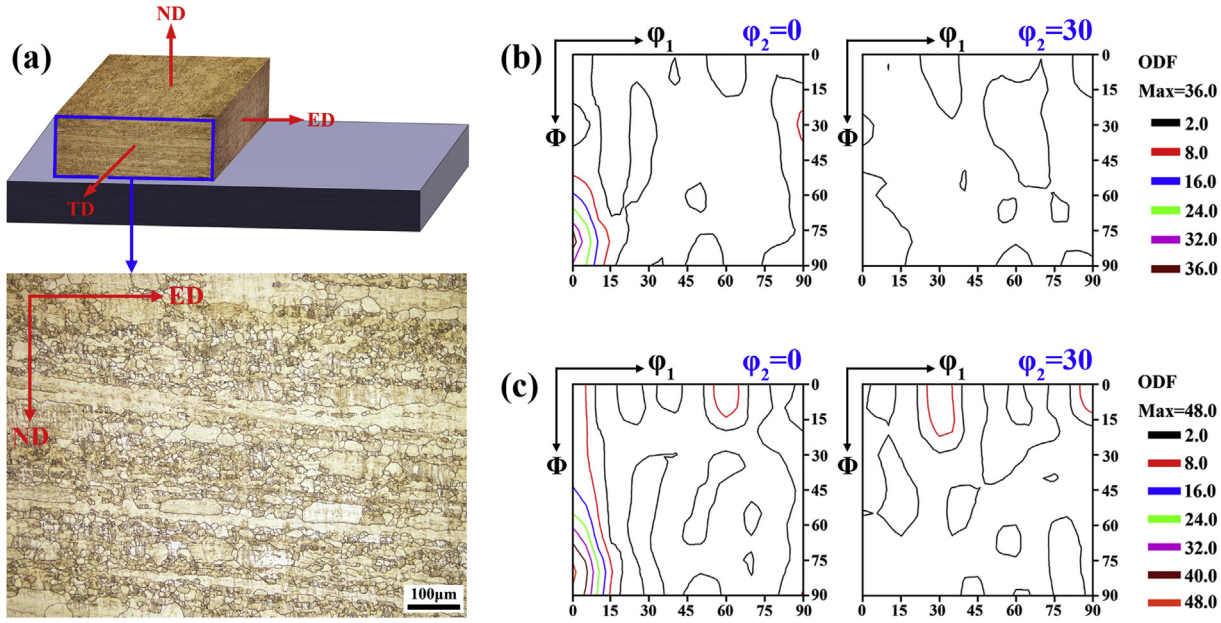

Fig. 1. Initial microstructure and textures of extruded Mg AZ31B plate. Optical micrograph in the ED-ND section (a), textures of skin layer (b) and center layer (c).

2.2. Mechanical testing

A series of experiments were performed in order to compare the mechanical behaviors of the extruded AZ31B Mg plate at quasi-static (~10^{-3} s^{-1}) and high strain rates (~10^{3} s^{-1}). Quasi-static compression tests were carried out up to failure along the ND. These tests were conducted in a conventional universal testing machine (Instron 5966). The cylindrical samples with the diameter of 5 mm and height of 10 mm were used. Compression tests at room temperature and high strain rate were performed up to failure or up to one "given" strain using a split Hopkinson pressure bar (SHPB). The details of this high strain rate test technique have been described in Ref. [29]. "Given" strain was achieved by "deformation frozen" technique which uses stop-ring of hardened steel surrounding the AZ31B Mg sample to interrupt the deformation process. Therefore, the microstructures were "frozen" at the "given" stages for subsequent observations. Design of the stop-ring and the schematic illustration of "deformation frozen" test are shown in Fig. 2(a, b).

As shown in Fig. 2 (c), cylindrical samples used for high strain rate tests were machined from the AZ31B Mg plate along ND. In order to achieve a wide range of strain rates, samples of three sizes were designed. Dynamic compression tests at strain rate ranges of 1068–3550 s^{-1} were performed on samples with the diameter of 8 mm and height of 6 mm. For strain rate ranges of 4737–5158 s^{-1}, samples have the diameter of 5.33 mm and height of 4 mm. For strain rate of 5647 s^{-1} and "deformation frozen" tests, samples have the diameter of 4 mm and height of 3 mm. The aspect ratio (length to diameter) of all cylindrical samples is 0.75:1. To check the repeatability and consistency of the results, at least three tests were conducted for both quasi-static and dynamic compression and the averages of the results were reported.

2.3. Microstructural examination

Textures of the samples, before and after high strain rate tests, were measured using XRD method. The XRD experiments were done employing Bruker D8 advance diffractometer with Cu Ka radiation and LynxEye 1D detector. Five incomplete pole figures (PFs), namely {0002}, {10-10}, {10-11}, {10-12} and {11-20} were measured firstly, then the ODF was calculated using the incomplete PFs. ODF was used to characterize the initial texture of the samples before compression tests. {0002} and {10-10} incomplete PFs were used to characterized the texture of samples after compression tests. For texture characterization of the samples after compression, the XRD data were taken from the compression plane of the samples, *i.e.*, the plane which is perpendicular to the compression direction.

EBSD technique was used to investigate the grain orientation and the type of twins in samples after high strain rate tests. EBSD was performed using a field emission scanning electron microscope FEI Nova NanoSEM 430 equipped with Oxford NORDLYS 2S detector. Data analysis was carried out using HKL-CHANNEL 5 data acquisition and analysis software. Sample preparation for EBSD investigations included grinding with 5000 SiC paper, mechanical polishing with a 0.25 μm diamond suspensions, and final electrochemical polishing for 60 s at 35 V using the modified AC2™ commercial electrolyte. The microstructure is represented by EBSD orientation maps and the texture by pole figures calculated from the EBSD orientation data.

The cylindrical compression samples were sectioned along the compression direction and subjected to metallography study by using OM. The sample surfaces for OM were polished to 2000 grit and finally polished with 0.5 μm diamond paste. Then the samples were chemically etched quickly for 3–5 s with a specially mixed solution of 5 g picric acid, 10 ml acetic acid, 100 ml anhydrous ethanol and 10 ml H_2O. Considering that Mg alloys are very active and susceptible to oxidation, deionized water was used to wash and clean samples during sample preparation. Samples for TEM characterization were cut along the compression plane of the compression samples using wire-cutting. These sections were then grounded to about 80 μm in thickness using SiC paper and then 3 mm disks were punched from the foils. The foils were electropolished using a twin-jet polisher to perforation by a solution of 3 vol% perchloric acid in ethanol. After electropolished the specimens were cleaned by ion milling for 0.5 h. Liquid nitrogen was applied during the ion milling. TEM observations were conducted by using FEI Tecnai G2 F20 operated at 200 kV.

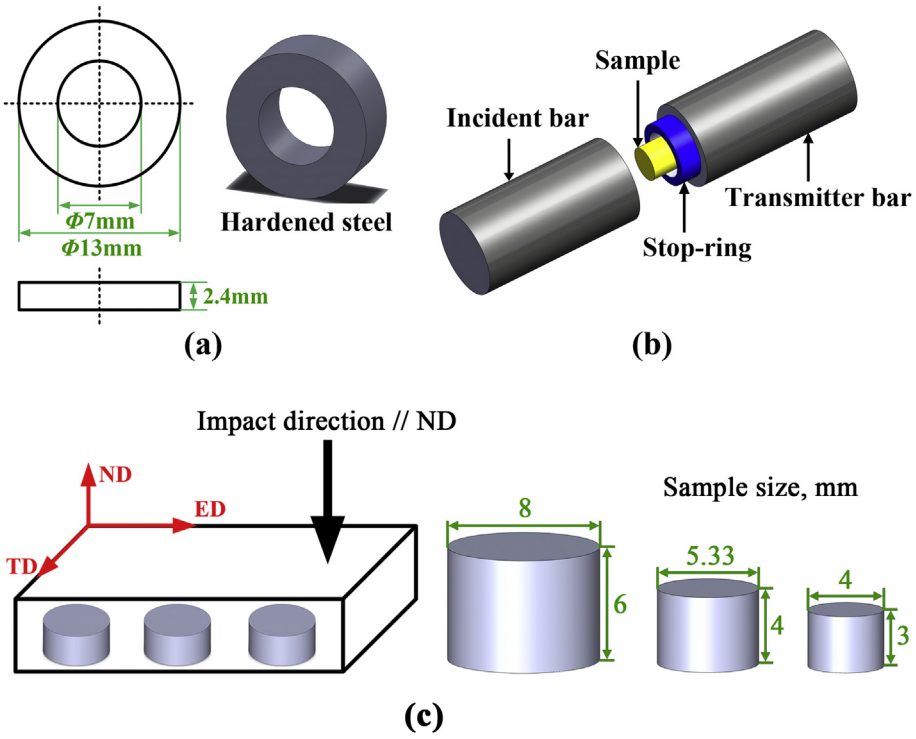

Fig. 2. (a) Design of stop-ring, (b) schematic illustration of the "deformation frozen" test and (c) sample sizes used for the split Hopkinson pressure bar test.

3. Results and discussions

3.1. Mechanical responses

Room temperature mechanical responses of AZ31B alloy under compression in the ND at quasi-static (~10^{-3} s^{-1}) and high strain rate (~10^{3} s^{-1}) are shown in Fig. 3 (a). As can be seen from Fig. 3 (a), the flow stress at high strain rate is always higher than that at quasi-static strain rate. Note that SHPB experiment does not accurately capture the elastic response [28], so the elastic portion of the mechanical curves has been removed. According to Ref [20], $\sigma_{0.005}$ (flow stresses corresponding to strains of $\varepsilon = 0.005$) is used in the present study as the mechanical response in the initial stage of plastic deformation. Obviously, the mechanical responses in Fig. 3 (a) can be classified into two types (Type-1 and Type-2). Type-1 and Type-2 represent the mechanical responses at strain rate ranges of 1068–3550 s^{-1} and 4737–5647 s^{-1}, respectively. The mechanical properties and corresponding deformation mechanisms are discussed as follows.

The dynamic mechanical responses of Type-1 exhibit sigmoidal hardening behavior. The flow stress and strain hardening are low at the initial deformation stage ($\varepsilon < 0.04$), and increase rapidly with increasing strain at the subsequent deformation stage ($\varepsilon > 0.04$). Many studies [15,27,30,31] have shown that the sigmoidal hardening behavior is typical of textured Mg and its alloys if deformation is dominated by {10–12} extension twinning. The dynamic mechanical responses of Type-2 exhibit power-law hardening behavior. The flow stress and strain hardening increase with the increase of strain at the initial deformation stage ($\varepsilon < 0.05$). The adiabatic softening occurred at the subsequent deformation stage ($\varepsilon > 0.05$), resulting in a decrease in flow stress but a significant enhancement in ductility (about two fold of that of Type-1). Fig. 3 (b, c) shows the schematic diagram of grain orientations of skin and center layers of the AZ31B Mg plate and the relative orientation of the compression axes with respect to the *c*-axes, which help to

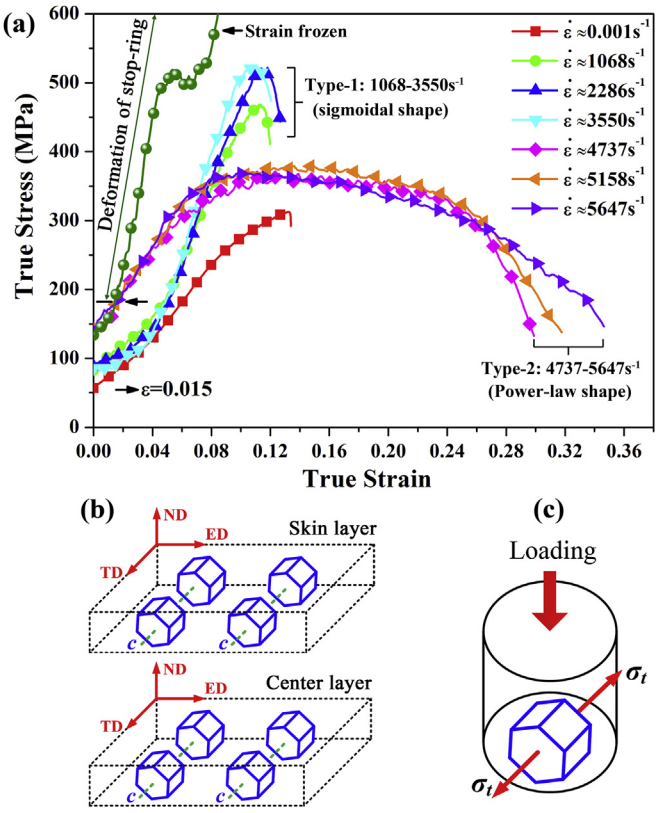

Fig. 3. Room temperature true stress-true strain responses of AZ31B alloy under compression in the ND at quasi-static (~10^{-3} s^{-1}) and high strain rate (~10^{3} s^{-1}). (a) Stress versus strain curves; (b) Schematic diagram of grain orientations of skin and center layers of AZ31B plate; (c) The relative orientation of the compression axes with respect to the *c*-axes for all tests in this investigation. Markers represent the values of "given" strain at which the test was interrupted for microstructural analysis.

understand the important deformation modes. The initial textures of AZ31B alloy are prismatic type and the main component is {11-20}⟨10-10⟩. If the AZ31B alloy is compressed along ND (*i.e.* the compression axis is perpendicular to the *c*-axes in most grains), this loading orientation places the *c*-axis in tension and {10–12} extension twinning is strongly favored at the early stages of deformation, causing grains to rotate ~86.3° and thus the *c*-axes to become closely aligned to the ND. The extension twinning plays an important role to mechanical behaviors of the materials.

In the case of mechanical responses of Type-1, the plastic deformation is dominated by {10–12} extension twinning at the initial deformation stage ($\varepsilon < 0.04$). The extension twinning has low CRSS and is insensitive to strain rate [20,32], which accounts for low flow stress and strain hardening. Previous studies [20,22,33] have proved extension twins nucleate and propagate quickly, often encompass the entire grain. Extension twinning formed completely at the initial deformation stage, causing *c*-axes to align with the compression axis. Thus the non-basal ⟨c+a⟩ dislocation slip become the dominant deformation mechanism together with twinning-induced formation of barriers to dislocation motion at the subsequent deformation stage ($\varepsilon > 0.04$), resulting in flow stress and strain hardening increase rapidly with increasing strain. In the case of mechanical responses of Type-2, the plastic deformation is dominated by non-basal ⟨c+a⟩ dislocation slip at the initial deformation stage ($\varepsilon < 0.05$). Dislocation multiplication and dislocations-dislocation interactions lead to flow stress and strain hardening increase with increasing strain. Adiabatic softening took place at the subsequent deformation stage ($\varepsilon > 0.05$), resulting in a decrease in flow stress but a significant increase in plastic strain.

As can be seen in Fig. 3 (a), the flow stress and strain hardening of Type-2 curves are higher than those of Type-1 curves at the initial deformation stage ($\varepsilon < 0.05$). The activation and transformation of {10-12} extension twinning significantly enhanced at higher strain rate [22,27]. Because the strain rate of Type-2 is higher than that of Type-1, a more intensive development of extension twinning possibly occurred in Type-2 than in Type-1. The non-basal ⟨c+a⟩ dislocation slip become the dominant deformation mechanism due to the rapid transformation of extension twinning at the initial deformation stage ($\varepsilon < 0.05$). The CRSS for non-basal ⟨c+a⟩ dislocation slip is significantly higher than that for extension twinning [20], which result in higher flow stress and strain hardening of Type-2 than those of Type-1 at the initial deformation stage ($\varepsilon < 0.05$). Adiabatic softening occurred during the last deformation stage of Type-2 curves due to more heat accumulation in samples under higher strain rate loading.

The yield stress (σ_y) is related to the CRSS of the various operating deformation mechanisms. Analyzing the variation of σ_y with strain rate can approximately infer the sensitivity of the CRSS of the operative deformation modes to strain rate. σ_y can be expressed by Ref. [20]:

$$\sigma_y = m\tau_0 + mkd^{-1/2} \quad (1)$$

where m is the Taylor factor, τ_0 is the CRSS for the operative slip systems, k is the microstructural shear stress intensity characterizing the grain boundary resistance to plastic deformation and d is the average grain size. Variation of yield strength ($\sigma_{0.005}$) and maximum strength (σ_{max}) of AZ31B alloy as a function of strain rate are shown in Fig. 4. Generally, $\sigma_{0.005}$ increases with the increase of strain rate. If the strain rate exceeds 3550 s^{-1}, a remarkable increase in $\sigma_{0.005}$ was found. The $\sigma_{0.005}$ at high strain rates is significantly higher than that at quasi-static strain rates, indicating the deformation model changed at the high strain rates. For the strain rate ranges of 1068–3550 s^{-1}, the plastic deformation is dominated by {10-12} extension twinning at the initial stage of deformation and

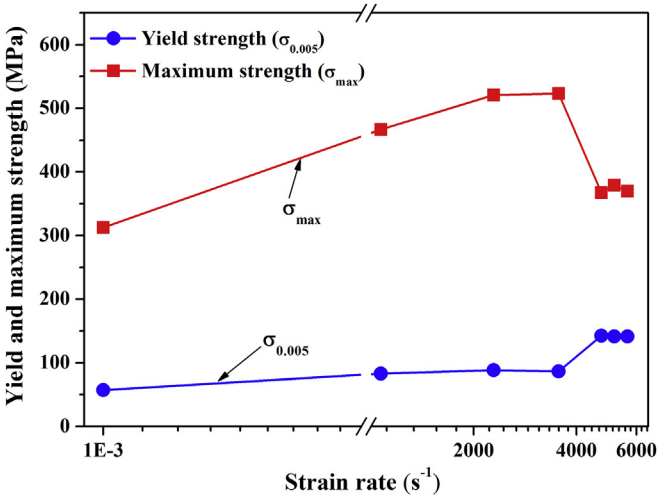

Fig. 4. Variation of the yield strength and the maximum strength as a function of strain rate.

$\sigma_{0.005}$ is nearly unchanged, indicating the CRSS for extension twining is strain rate independent [20,32]. For the strain rate ranges of 4737–5647 s^{-1}, the deformation mechanism is mainly non-basal ⟨c+a⟩ dislocation slip and $\sigma_{0.005}$ is almost constant, demonstrating the CRSS for non-basal ⟨c+a⟩ dislocation slip is insensitive to strain rate [20]. In addition, the $\sigma_{0.005}$ at strain rate ranges of 4737–5647 s^{-1} is higher than that at strain rate ranges of 1068–3550 s^{-1}, indicating the CRSS for non-basal ⟨c+a⟩ dislocation slip is higher than that for {10–12} extension twinning. With the increase of strain rate, the σ_{max} increases firstly and then decreases after reaching the peak value. As can be seen from Fig. 4, for the strain rate ranges of 0.001–3550 s^{-1}, σ_{max} increases obviously with the increase of strain rate due to continuous strain hardening. If the strain rate exceeds 3550 s^{-1}, σ_{max} decreases significantly due to occurrence of adiabatic softening.

The strain hardening rate ($d\sigma/d\varepsilon$) at quasi-static and high strain rates (1068–5647 s^{-1}) compression tests in the ND are shown in Fig. 5. The $d\sigma/d\varepsilon$ is defined as the rate of change of true stress-true strain curve and is calculated by the numerical differentiation of the true stress-true strain data in Fig. 3 (a). The variations of $d\sigma/d\varepsilon$ curves in Fig. 5 can be categorized into two groups. The variations of $d\sigma/d\varepsilon$ at the strain rate ranges of 1068–3550 s^{-1} and 4737–5647 s^{-1} are belong to Type-1 and Type-2, respectively. The

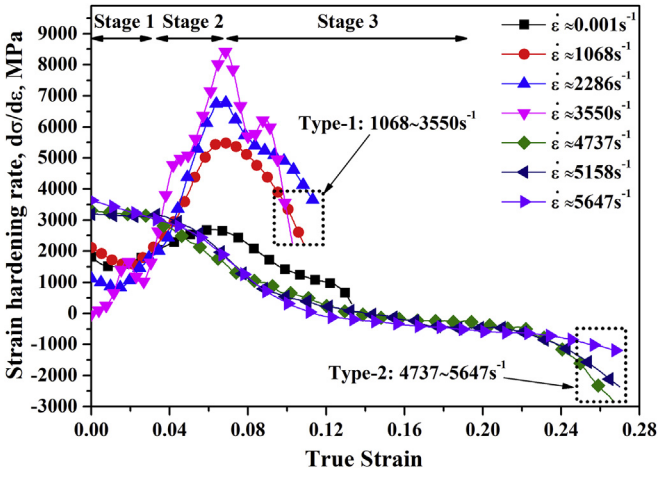

Fig. 5. Variations of strain hardening rate as a function of true strain.

$d\sigma/d\varepsilon$ of Type-1 can be divided into three stages in the plastic regime. Stage 1 ($\varepsilon < 0.04$): a very low $d\sigma/d\varepsilon$; Stage 2 ($0.04<\varepsilon < 0.07$): $d\sigma/d\varepsilon$ increases rapidly with the increase of strain; Stage 3 ($\varepsilon > 0.07$): $d\sigma/d\varepsilon$ decreases with the increase of strain. The very low $d\sigma/d\varepsilon$ in stage 1 is responsible for the formation and spreading of {10−12} extension twinning. The higher $d\sigma/d\varepsilon$ in stage 2 is responsible for the activation of the non-basal ⟨c+a⟩ dislocation slip as well as the twinning-induced formation of barriers to dislocation motion. The decreasing $d\sigma/d\varepsilon$ in stage 3 is responsible for occurrence of dynamic recovery (dislocation-dislocation interactions).

The $d\sigma/d\varepsilon$ of Type-2 is similar to that of Type-1, which can be divided into three stages as well. Stage 1 ($\varepsilon < 0.05$): $d\sigma/d\varepsilon$ is basically unchanged with the increase of strain; Stage 2 ($0.05 < \varepsilon < 0.1$): $d\sigma/d\varepsilon$ decreases obviously with the increase of strain; Stage 3 ($\varepsilon > 0.1$): $d\sigma/d\varepsilon$ decreases gradually with the increase of strain. The nearly constant $d\sigma/d\varepsilon$ in stage 1 is responsible for the non-basal ⟨c+a⟩ dislocation slip as well as the twinning-induced formation of barriers to dislocation motion. The rapid decrease of $d\sigma/d\varepsilon$ in Stage 2 is responsible for occurrence of dynamic recovery. The gradual decrease of $d\sigma/d\varepsilon$ in stage 3 is responsible for occurrence of adiabatic softening.

Analysis of strain hardening rate suggests that: $d\sigma/d\varepsilon$ is low if plastic flow is dominated by extension twinning; $d\sigma/d\varepsilon$ increases significantly with the increase of strain if plastic flow is dominated by non-basal ⟨c+a⟩ dislocation slip together with twin-dislocation interaction; $d\sigma/d\varepsilon$ decreases gradually with the increase of strain if adiabatic softening or dynamic recovery takes place.

3.2. Microstructure and texture evolution

To further investigate the deformation mechanism at the initial stage, the “deformation frozen” test and its corresponding microstructural analysis were carried out. Fig. 6 presents the microstructures and textures in AZ31B samples deformed upon strain of 1.5%. The stress-strain curve of “deformation frozen” test has been shown in Fig. 3 (a). The optical micrographs from longitudinal sections of samples with magnification of 200× and 1000× are shown in Fig. 6 (a, b). It demonstrates that considerable amount of deformation twins formed and the twin boundaries are curving. The textures of samples after dynamically compressed are shown in Fig. 6 (c), which indicates the development of a double-peak {0002} basal texture. The basal poles are tilted away by almost 20° and 25° from ND toward TD. In other words, the texture changed from initial prismatic type to double-peak basal texture after dynamically compressed. Considering the splitting of basal poles in the pole figures (Fig. 6 (c)), it is reasonable to propose that the combination of twinning and non-basal ⟨c+a⟩ slip could result in the formation of the double-peak basal texture [6,34,35]. In fact, it is difficult to determine which deformation mechanism plays a major role in the present study. However, for the plastic deformation at the initial stage, non-basal ⟨c+a⟩ slip is difficult to be activated due to its higher CRSS, thus it seems to be logical to suggest that twinning is the dominant deformation mechanism in the earlier deformation stage.

The deformation mechanism can be well understood by analyzing the microstructural evolution in AZ31B samples after dynamically compressed. Fig. 7 presents the microstructural evolution of AZ31B alloy under quasi-static and dynamic (1068−5158 s^{-1}) compression in the ND. Fig. 7(a–c) shows the optical micrographs of samples after compressed at quasi-static strain rate. It is clear that a large number of deformation twinning formed and their distribution is inhomogeneous. Some of the twins are thick and coarse. The twin boundaries are not straight and twin intersections are found apparently. Judging from the morphologies, these deformation twins should be {10-12} extension twinning. Fig. 7(d–f) shows the optical micrographs from

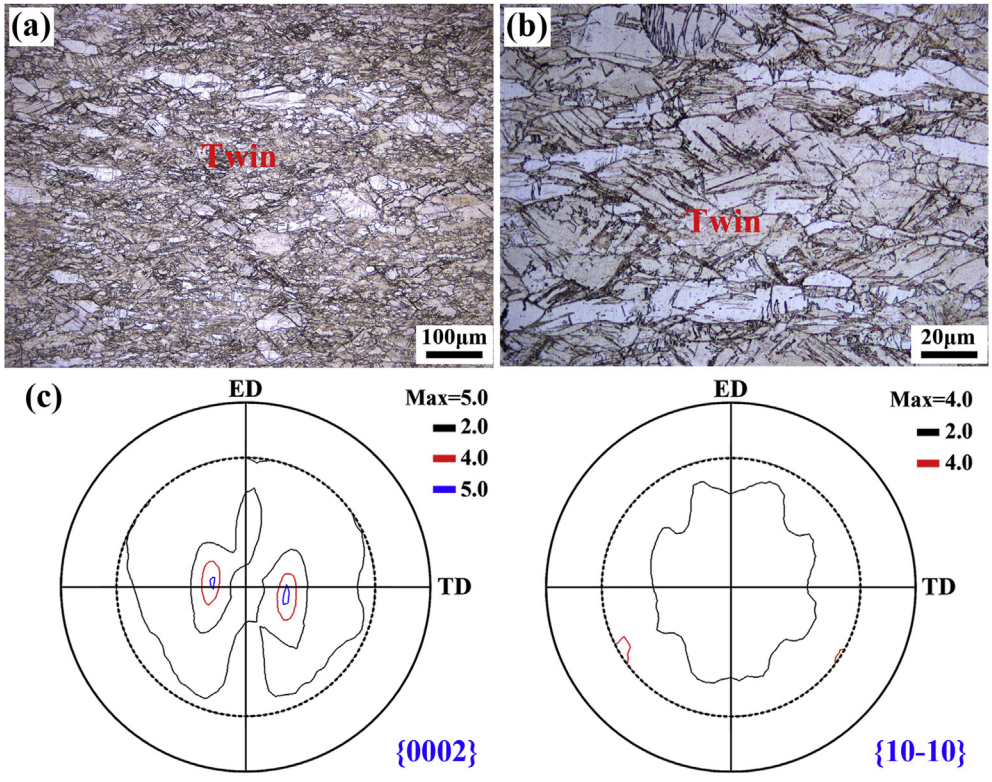

Fig. 6. Microstructure and texture in AZ31B samples dynamically compressed upon strain of 1.5%. Optical micrographs of 200× magnification (a) and 1000× magnification (b); {0002} and {10-10} incomplete pole figures (c).

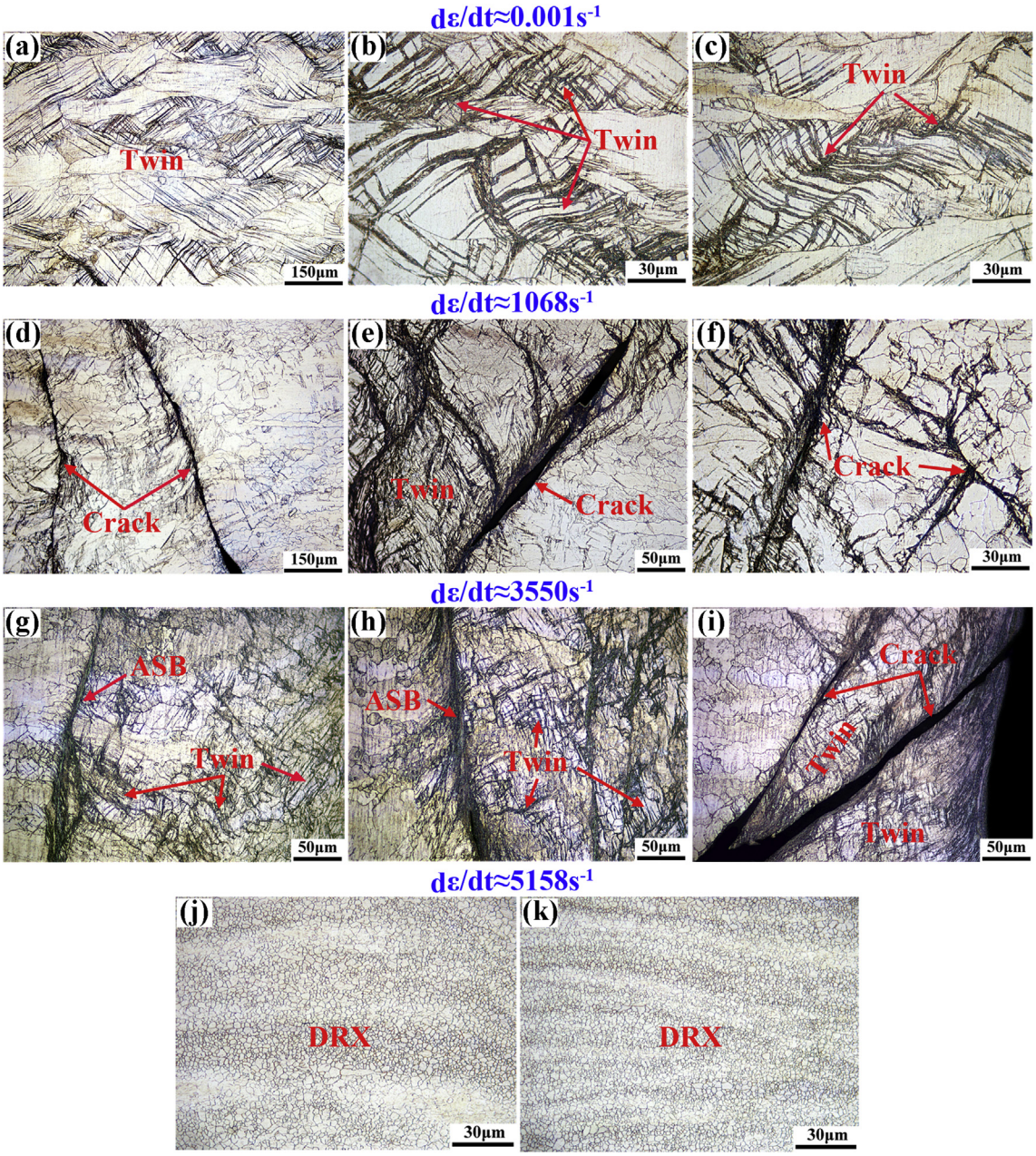

Fig. 7. Microstructural evolutions of AZ31B alloy under compression in the ND at quasi-static and high strain rate. (a–c) $d\varepsilon/dt \approx 0.001\ s^{-1}$; (d–f) $d\varepsilon/dt \approx 1068\ s^{-1}$; (g–i) $d\varepsilon/dt \approx 3550\ s^{-1}$; (j, k) $d\varepsilon/dt \approx 5158\ s^{-1}$.

longitudinal sections of AZ31B samples after dynamically compressed at strain rate of 1068 s^{-1}. It can be seen that the localization of deformations occurred during deformation process. Besides, cracks formed and propagated in base metal. The main cracks are accompanied by a large number of secondary cracks and lots of deformation twins distributed in the vicinity the cracks. Fig. 7(g–i) presents the optical micrographs of the longitudinal sections of samples after dynamically compressed at strain rate of 3550 s^{-1}. Similarly, deformation localization commenced during deformation and the deformed microstructures were characterized by adiabatic shear bands (ASBs) and cracks. Around the ASBs and cracks there are intensive deformation twins. Compared with the deformed microstructures at strain rate of 1068 s^{-1} (Fig. 7(d–f)), the formation and development of ASBs and cracks are more intensive if the strain rate increased to 3550 s^{-1}. In addition, Fig. 7(h) shows that ASB formed prior to crack, and then developed into cracks. Fig. 7(j, k) presents the optical micrographs of samples after dynamically compressed at strain rate of 5158 s^{-1}. It is found that deformed microstructures are fully composed of fine grains produced by DRX. The grain sizes are about 2–5 μm. As mentioned above, adiabatic softening took place at the later deformation stage ($\varepsilon > 0.05$) for Type-2 mechanical curves (strain rate ranging from 4737 s^{-1} to 5647 s^{-1}). From the microstructures of dynamically compressed sample, it can be inferred that DRX occurred during dynamic compression. In other words, adiabatic softening of the material is related to occurrence of DRX.

The microstructural evolution in Fig. 7 demonstrates that the deformed microstructures and the responses of material to various strain rate loadings are significantly different. The microstructures under quasi-static compression are mainly characterized by

deformation twinning, *i.e.*, the plastic deformation is mainly conducted by twinning. Deformation localization took place during the dynamic compression (1068–3550 s^{-1}). In this case, the deformed microstructures are mainly characterized by ASBs and cracks. If strain rate increased to 5158 s^{-1}, DRX took place and the ductility was enhanced significantly.

In order to identify the type and distribution of deformation twins in the microstructure of AZ31B alloys after high strain rate test, EBSD analysis was conducted. The inverse pole figure (IPF) maps and image quality (IQ) maps of AZ31B alloy after high strain rate tests are shown in Fig. 8. It is difficult for EBSD technique to analyze sample after large and high strain rate deformation, the white areas in Fig. 8 are regions that is not recognized by EBSD. However, the data in Fig. 8 is sufficient to account for the type and distribution of twins in the deformed AZ31B Mg samples. It is obvious that twinning occurred in all samples after dynamically

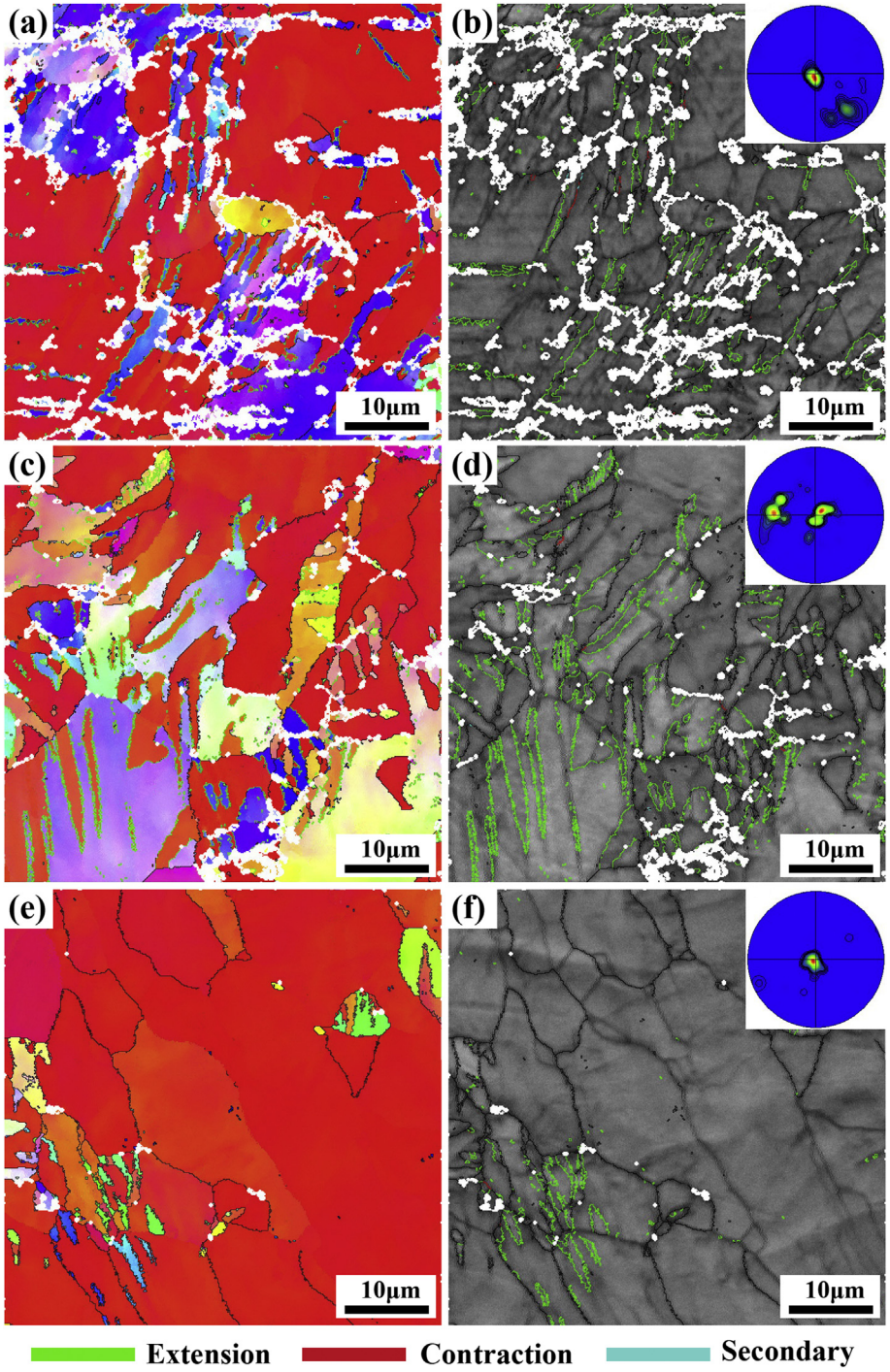

Fig. 8. Inverse pole figure (IPF) maps and image quality (IQ) maps of AZ31B alloy showing the microstructure and twins type formed after high strain rate test. (a–b) $d\varepsilon/dt \approx 1068\ s^{-1}$; (c–d) $d\varepsilon/dt \approx 2286\ s^{-1}$; (e–f) $d\varepsilon/dt \approx 3550\ s^{-1}$. The {0002} pole figures calculated from the EBSD data for the regions shown in Fig. 8 (a, c, e) are illustrated in the upper right corner of Fig. 8 (b, d, f) respectively. Extension twin boundaries (86° ⟨11-20⟩ ± 5°) are colored in lime green, contraction twin boundaries (56° ⟨11-20⟩ ± 5°) are colored in red, and secondary twin boundaries (38° ⟨11-20⟩ ± 5°) are colored in olive. (For interpretation of the references to color in this figure legend, the reader is referred to the web version of this article.)

compressed (1068–3550 s^{-1}). Three types of twins that formed in the samples during high strain rate test are marked in Fig. 8. As it is observed, the main twins are {10-12} extension twins (shown in lime green). Besides, very few {10-11} contraction twins (shown in red) and {10-11}-{10-12} secondary twins (shown in olive) formed, which are difficult to be found. The fraction of {10-12} extension twins is larger than those of other twins (contraction and secondary) which can be ascribed to its favorable orientation and lower CRSS that makes it a dominant deformation mode in AZ31B alloys. In addition, the {0002} pole figures calculated from the EBSD data for the regions shown in Fig. 8(a, c, e) are illustrated in the insets of Fig. 8(b, d, f) respectively. It can be seen {0002} basal texture formed after dynamic compression because of extensive formation of {10-12} extension twins. Furthermore, the basal texture intensity increases significantly with the increase in strain rate, indicating that twinning is enhanced at high strain rate. Because EBSD

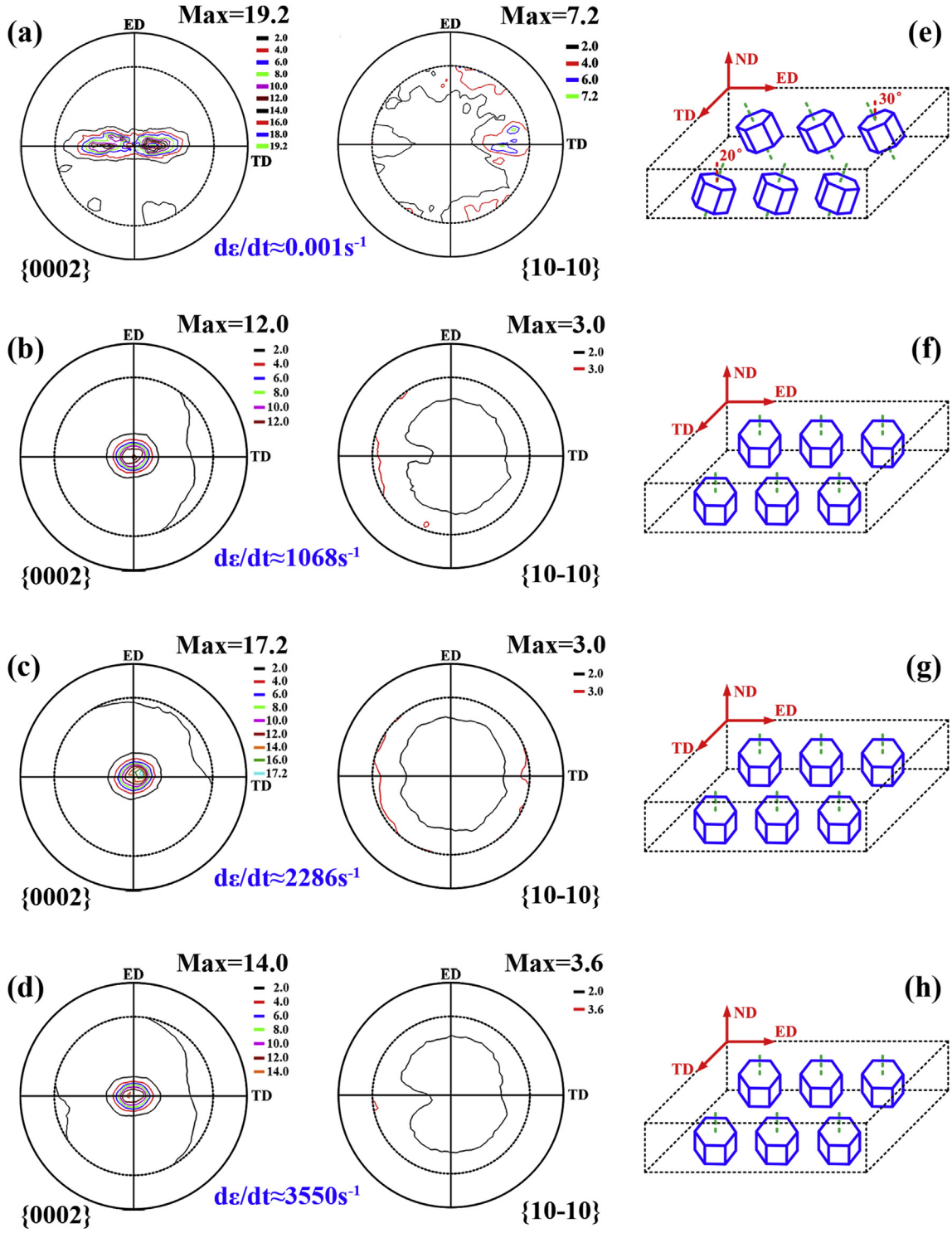

Fig. 9. Texture evolutions of AZ31B alloy after compressed in the ND at quasi-static and high strain rate. (a) $d\varepsilon/dt \approx 0.001\ s^{-1}$; (b) $d\varepsilon/dt \approx 1068\ s^{-1}$; (c) $d\varepsilon/dt \approx 2286\ s^{-1}$; (d) $d\varepsilon/dt \approx 3550\ s^{-1}$.

technique only can detect the local region of the deformed samples, it is difficult to determine the exact fraction of the extension twins from Fig. 8. However, the evolution of {0002} pole figures of detect region in samples indicate the fraction of extension twins possibly increase with the increase of strain rate. The formation and development of {10-12} extension twins provide substantial barriers to dislocation motion, resulting in high stress and strain hardening.

It is well known that texture analysis is a powerful tool to study the microstructural change and the deformation mechanism. To further reveal the deformation mechanism under high strain rate compression, XRD texture measurements of deformed samples were conducted, which give a good statistical description of the macrotexture. The compression plane (*i.e.*, the plane perpendicular to the impact direction), was taken into account for texture measurements. Texture evolutions of samples under compression in the ND at quasi-static and high strain rates (1068–3550 s^{-1}) are shown in Fig. 9. Fig. 9(a) shows the texture of samples after quasi-static compression as a reference to the dynamic compression. As can be seen, a weak {0002} basal texture formed, *c*-axes in most grains rotated around ED toward ND and the angle between *c*-axis and ND is about 20°–30°, indicating {10-12} extension twins occurred only to a certain extent. The microstructures in sample after quasi-static compression in Fig. 7(a–c) also confirmed substantial formation of extension twins, which is consistent with the texture analysis. Fig. 9(b–d) presents the textures in samples after dynamically compressed at strain rate ranges of 1068–3550 s^{-1}. It is observed that the initial prismatic texture converts to a strong {0002} basal texture, indicating {10-12} extension twinning formed extensively. As a result, most orientations of parent grain transformed into orientations of extension twinning. Fig. 9(e–h) shows the schematic diagrams of grain orientations after quasi-static and dynamic compression to assist in illustrating the textures shown in Fig. 9(a–d).

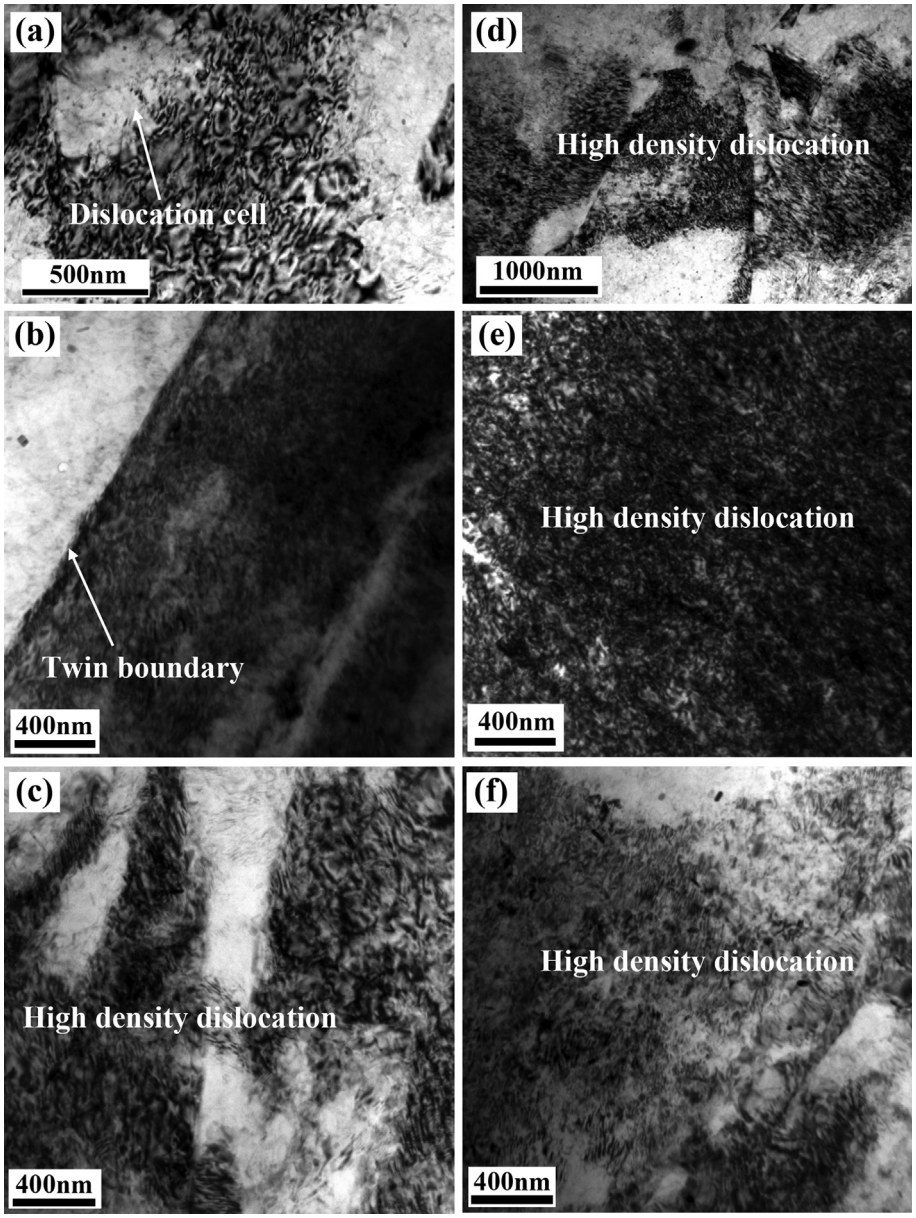

Fig. 10. Bright field TEM micrographs of AZ31B alloy under compression in the ND at strain rate of 1068 s^{-1}. (a) Dislocation cell; (b) Accumulation and pile-ups of dislocations at the twin boundary; (c–f) High density dislocations observed in different regions.

The formation of {0002} basal texture is related to a combination of both {10-12} extension twinning and basal ⟨a⟩ slip. In general, extension twinning plays a predominant role under such conditions. It is noted that the maximum intensities of {0002} and {10-10} PFs in Fig. 9(a–d) exhibit no obvious regularities, which may be resulted from the local texture inhomogeneity in materials. However, texture evolution in samples after dynamic compression shows a strong regularity. A strong {0002} basal texture formed, indicating that high strain rate enhances the activation of {10–12} extension twinning dramatically. Consistently, previous studies [20,22,36,37] have confirmed that the nucleation and development of extension twins are dramatically enhanced at high strain rate (the order of ~10^3 s^{-1} or above). In fact, extension twins form and propagate very soon, often encompassing the entire grain [15].

Dynamic mechanical behavior and deformation mechanism of AZ31B alloy can be understood by analyzing the texture evolution in Fig. 9 together with the microstructural evolution in Fig. 7 and EBSD results in Fig. 8. If the samples are dynamically compressed at strain ranges of 1068–3550 s^{-1}, {10-12} extension twinning form and develop quickly till encompass the entire grain during the initial deformation stage, causing the *c*-axes to align with the ND. In the later deformation stage, non-basal ⟨c+a⟩ dislocation slip becomes the dominant deformation mechanism. As a result, multiplication of ⟨c+a⟩ dislocation combined with impediment of twins to the motion of dislocation result in obvious increases in strain hardening and flow stress. If the samples are dynamically compressed at strain rate ranges of 4737–5647 s^{-1}, DRX take place, leading to a decrease in flow stress but a significant enhancement in ductility.

3.3. Dislocation substructure and microhardness analysis

To further understand the macroscopic mechanical behaviors of the material and their corresponding deformation mechanisms, TEM observations were carried out. Fig. 10 presents the bright field TEM micrographs of AZ31B Mg alloy after compressed in the ND at strain rate of 1068 s^{-1}. Fig. 10 shows the formation of dislocation cell (Fig. 10(a)), accumulation and pile-ups of dislocations at the twin boundary (Fig. 10(b)), and the high density dislocations in different regions (Fig. 10(c–f)). Mg and its alloy has relatively low stacking fault energy (SFE, the SFE of pure Mg is 60–78 mJ/m^2). In general, the dislocation cell structure is difficult to form and be observed if deformed at quasi-static and low strain rate. On the contrary, high density dislocations could be produced under high strain rate (~10^3 s^{-1}) deformation, and the interactions of dislocation-dislocation are enhanced. Thus dislocation-dislocation interactions and recovery processes most likely result in the formation of the dislocation cell.

Fig. 11 presents the bright field TEM micrographs of AZ31B alloy under compression in the ND at strain rate of 3550 s^{-1}. The deformation twin, dislocation accumulation and pile-up inside twin (Fig. 11(a)) as well as the high density dislocations in different regions (Fig. 11(b–d)) are shown. It is noted that the presence of deformation twin is only observed in Fig. 11(a). Although the mechanical behaviors (Fig. 3), microstructure analysis (Figs. 7 and 8) and the texture evolution (Fig. 9) strongly indicate the occurrence

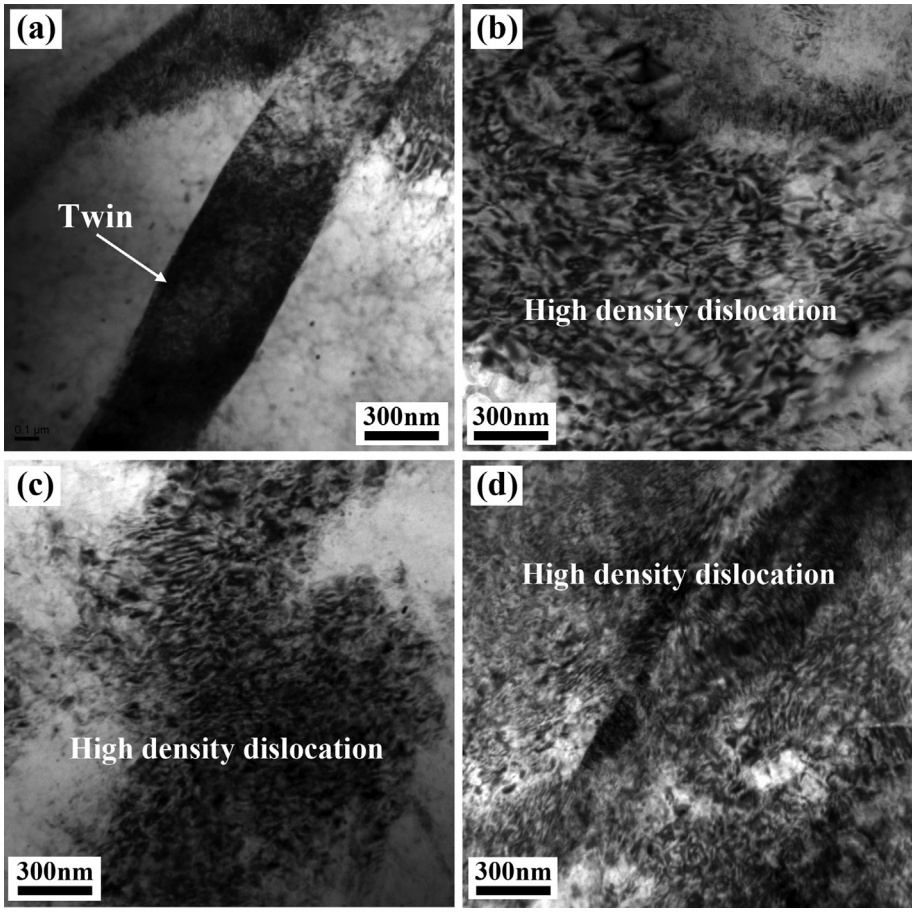

Fig. 11. Bright field TEM micrographs of AZ31B alloy under compression in the ND at strain rate of 3550 s^{-1}. (a) Deformation twin and dislocation accumulation and pile-up inside twin; (b–d) High density dislocations observed in different regions.

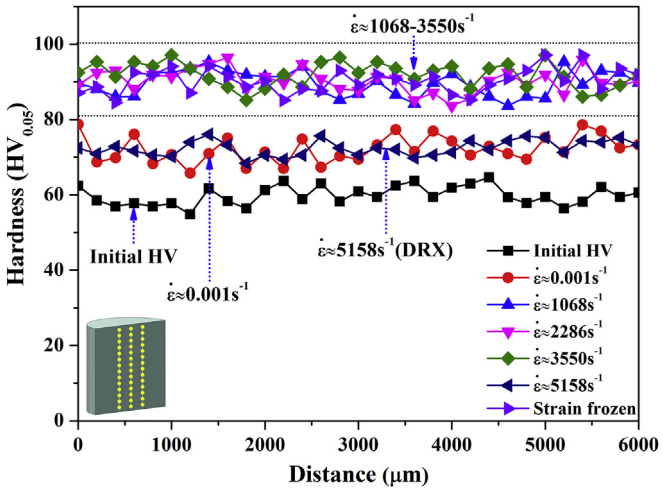

Fig. 12. Variations of Vickers microhardness of AZ31B alloy compressed at quasi-static and high strain rate.

of extension twinning, our TEM observations of the microstructures deformed at high strain rates (1068 s^{-1} and 3550 s^{-1}) do not reveal well-defined twins. This is because extension twinning formed and developed quickly at high strain rate deformation, and almost consumed all the grains. As a consequence, twin is hard to be identified under TEM observations. This characteristic has also been reported by other researchers [22,26,27,37]. It is concluded from Figs. 10 and 11 that a high density of dislocations is produced and the dislocation multiplication and interaction take place upon high strain rate deformation in AZ31B samples. High density of dislocations is the main characteristic of the microstructure, indicating dislocations slip become an important mechanism of plastic deformation during the latter deformation stage. The dislocation-dislocation interactions and dislocation-twin interactions contribute to a sharp increase in strain hardening and flow stress [24,27,28].

In general, the relationship between flow stress (τ) and dislocation density (ρ) can be expressed as [38]:

$$\tau = \tau_0 + \alpha G b \sqrt{\rho} \quad (2)$$

where τ_0 is the shear force to make dislocation motion if no other dislocations exist; α is constant and its value is ranging from 0.3 to 0.6; G is the shear modulus and b is the burgers vector. Equation (2) indicates the flow stress is proportional to the square root of dislocation density.

For metallic materials, the density of dislocation has key influences on microhardness. The variations of dislocation in AZ31B samples after deformation can be inferred by measuring and analyzing the microhardness of the deformed samples. Vickers microhardness variations of AZ31B samples compressed at quasi-static and high strain rate (1068–5158 s^{-1}) are shown in Fig. 12. Measurements of microhardness were conducted on the longitudinal section of the deformed samples and the average values were reported. The initial microhardness of AZ31B is 60 HV, and microhardness of samples compressed at quasi-static strain rate is 72 HV. Microhardness of samples after high strain rate (1068–3550 s^{-1}) compression and "deformation frozen" tests are very close (90–92 HV). Microhardness of samples compressed at strain rate of 5158 s^{-1} is 72 HV, which is consistent with that of samples compressed at quasi-static strain rate. It is found that the microhardness of samples compressed at quasi-static and high strain rate is higher than the initial microhardness. The highest microhardness value is found at the strain rate range of 1068–3550 s^{-1}. If the strain rate exceeds 3550 s^{-1} and continues to increase, microhardness of samples decreases.

The deformed samples exhibit different microhardness, reflecting the changes in microstructures (mainly dislocation density) during plastic deformation. Samples dynamically compressed at strain rate ranges of 1068–3550 s^{-1} have the highest microhardness, indicating the maximum dislocation density has generated in this situation. The dislocation density can refer to TEM observations in Fig. 10 (1068 s^{-1}) and Fig. 11 (3550 s^{-1}). The microhardness of samples deformed at the initial deformation stage is basically the same as that of samples after high strain rate deformation (1068–3550 s^{-1}). This indicates that a large number of dislocations have generated at the initial deformation stage and dynamic deformation can promote the increase of dislocation density. If strain rate increases to 5158 s^{-1}, DRX will take place, leading to a decrease in dislocation density as well as a decrease in microhardness correspondingly.

4. Conclusions

The dynamic mechanical properties of extruded AZ31B Mg plate under compression in the ND at room temperature are studied. The corresponding deformation mechanisms and microstructural evolutions have been elucidated by the examination and analysis of microstructures in deformed samples. The following conclusions can be drawn from this work.

(1) The mechanical responses exhibit sigmoidal hardening and power-law hardening behaviors under high strain rate compression. For strain rate ranges of 1068–3550 s^{-1}, the mechanical behaviors show sigmoidal hardening response. The strain hardening and flow stress are relative low at the initial deformation stage, and increase sharply with the increasing strain at the following deformation stage. For the strain rate ranges of 4737–5647 s^{-1}, the mechanical behaviors show power-law hardening response. The strain hardening and flow stress increase gradually at the initial deformation stage. Adiabatic softening takes place during the subsequent deformation stage, resulting in an obvious decrease in flow stress but a significant enhancement in plastic strain.

(2) It is found that the prismatic type textures of the skin layer and center layer in AZ31B plate determine the dynamic mechanical behaviors. The sigmoidal hardeningbehaviors are resulted from the formation and development of extension twinning at the initial deformation stage. The non-basal ⟨c+a⟩ dislocation slip dominated the deformation at the subsequent deformation stage. The power-law hardening behaviors are resulted from that the non-basal ⟨c+a⟩ dislocation slip and occurrence of dynamic recrystallization dominated the initial deformation and the following deformation, respectively.

(3) It is found that the CRSS for {10-12} extension twinning and non-basal ⟨c+a⟩ dislocation slip are insensitive to strain rate, but the latter CRSS is significantly higher than the former one. If the plastic deformation is dominated by extension twinning, flow stress keeps nearly unchanged with increasing strain rate; If plastic deformation is dominated by non-basal ⟨c+a⟩ dislocation slip, flow stress increases with increasing strain rate.

Acknowledgements

This work was supported by National Natural Science

Foundation of China under Contract No: 51471090. Assistance from Prof. Li Meng with the discussion of microtexture (EBSD) and macrotexture (XRD) analysis was appreciated.

References

[1] B.L. Mordike, T. Ebert, Magnesium: properties-applications-potential, Mater. Sci. Eng. A 302 (2001) 37–45.
[2] M. Easton, A. Beer, M. Barnett, C. Davies, G. Dunlop, Y. Durandet, S. Blacket, T. Hilditch, P. Beggs, Magnesium alloy applications in automotive structures, JOM 60 (2008) 57–62.
[3] S.N. Mathaudhu, E.A. Nyberg, Magnesium alloys in U.S. military applications: past, current and future solutions, Magnes. Technol. (2010) 71–76.
[4] J.A. Del valle, F. Carreno, O.A. Ruano, Influence of texture and grain size on work hardening and ductility in magnesium-based alloys processed by ECAP and rolling, Acta Mater. 54 (2006) 4247–4259.
[5] Y.Q. Cheng, Z.H. Chen, Anisotropy of deformation behavior of AZ31 magnesium alloy sheets, Adv. Mater. Res. 314–316 (2011) 1121–1125.
[6] S.R. Agnew, M.H. Yoo, C.N. Tomé, Application of texture simulation to understanding mechanical behavior of Mg and solid solution alloys containing Li or Y, Acta Mater. 49 (2001) 4277–4289.
[7] S.R. Agnew, C.N. Tomé, D.W. Brown, T.M. Holden, S.C. Vogel, Study of slip mechanisms in a magnesium alloy by neutron diffraction and modeling, Scr. Mater. 48 (2003) 1003–1008.
[8] M.R. Barnett, Z. Keshavarz, A.G. Beer, D. Atwell, Influence of grain size on the compressive deformation of wrought Mg-3Al-1Zn, Acta Mater. 52 (2004) 5093–5103.
[9] J. Koike, Enhanced deformation mechanisms by anisotropic plasticity in polycrystalline Mg alloys at room temperature, Metall. Mater. Trans. A 36A (2005) 1689–1696.
[10] X.Y. Lou, M. Li, R.K. Boger, S.R. Agnew, R.H. Wagoner, Hardening evolution of AZ31B Mg sheet, Int. J. Plast. 23 (2007) 44–86.
[11] L. Jiang, J.J. Jonas, A.A. Luo, A.K. Sachdev, S. Godet, Influence of {10-12} extension twinning on the flow behavior ofAZ31 Mg alloy, Mater. Sci. Eng. A 445–446 (2007) 302–309.
[12] Y. Chino, K. Kimura, M. Mabuchi, Twinning behavior and deformation mechanisms of extruded AZ31 Mg alloy, Mater. Sci. Eng. A 486 (2008) 481–488.
[13] P. Cizek, M.R. Barnett, Characteristics of the contraction twins formed close to the fracture surface in Mg-3Al-1Zn alloy deformed in tension, Scr. Mater. 59 (2008) 959–962.
[14] M.R. Barnett, Z. Keshavarz, A.G. Beer, X. Ma, Non-Schmid behaviour during secondary twinning in a polycrystalline magnesium alloy, Acta Mater. 56 (2008) 5–15.
[15] M. Knezevica, A. Levinson, R. Harris, R.K. Mishra, R.D. Doherty, S.R. Kalidindi, Deformation twinning in AZ31: influence on strain hardening and texture evolution, Acta Mater. 58 (2010) 6230–6242.
[16] T.A. Samman, G. Gottstein, Dynamic recrystallization during high temperature deformation of magnesium, Mater. Sci. Eng. A 490 (2008) 411–420.
[17] A. Galiyev, R. Kaibyshev, G. Gottstein, Correlation of plastic deformation and dynamic recrystallization in magnesium alloy ZK60, Acta Mater. 49 (2001) 1199–1207.
[18] Z. Keshavarz, M.R. Barnett, EBSD analysis of deformation modes in Mg-3Al-1Zn, Scr. Mater. 55 (2006) 915–918.
[19] M.T. Tucker, M.F. Horstemeyer, P.M. Gullett, H.E. Kadiri, W.R. Whittington, Anisotropic effects on the strain rate dependence of a wrought magnesium alloy, Scr. Mater. 60 (2009) 182–185.
[20] I. Ulacia, N.V. Dudamell, F. Gálvez, S. Yi, M.T. Pérez-Prado, I. Hurtado, Mechanical behavior and microstructural evolution of a Mg AZ31 sheet at dynamic strain rates, Acta Mater. 58 (2010) 2988–2998.
[21] G. Wan, B.L. Wu, Y.D. Zhang, G.Y. Sha, C. Esling, Anisotropy of dynamic behavior of extruded AZ31 magnesium alloy, Mater. Sci. Eng. A 527 (2010) 2915–2924.
[22] N.V. Dudamell, I. Ulacia, F. Gálvez, S. Yi, J. Bohlen, D. Letzig, I. Hurtado, M.T. Pérez-Prado, Twinning and grain subdivision during dynamic deformation of a Mg AZ31 sheet alloy at room temperature, Acta Mater. 59 (2011) 6949–6962.
[23] G. Wan, B.L. Wu, Y.H. Zhao, Y.D. Zhang, C. Esling, Strain-rate sensitivity of textured Mg-3.0Al-1.0Zn alloy (AZ31) under impact deformation, Scr. Mater. 65 (2011) 461–464.
[24] H. Asgari, J.A. Szpunar, A.G. Odeshi, L.J. Zeng, E. Olsson, Experimental and simulation analysis of texture formation and deformation mechanism of rolled AZ31B magnesium alloy under dynamic loading, Mater. Sci. Eng. A 618 (2014) 310–322.
[25] F. Feng, S.Y. Huang, Z.H. Meng, J.H. Hu, Y. Lei, M.C. Zhou, D. Wu, Z.Z. Yang, Experimental study on tensile property of AZ31B magnesium alloy at different high strain rates and temperatures, Mater. Des. 57 (2014) 10–20.
[26] K.E. Prasad, B. Li, N. Dixit, M. Shaffer, S.N. Mathaudhu, K.T. Ramesh, The dynamic flow and failure behavior of magnesium and magnesium alloys, JOM 66 (2014) 291–304.
[27] N. Dixit, K.Y. Xie, K.J. Hemker, K.T. Ramesh, Microstructural evolution of pure magnesium under high strain rate loading, Acta Mater. 87 (2015) 56–67.
[28] A. Pandey, F. Kabirian, J.H. Hwang, S.H. Choi, A.S. Khan, Mechanical responses and deformation mechanisms of an AZ31Mg alloy sheet under dynamic and simple shear deformations, Int. J. Plast. 68 (2015) 111–131.
[29] W.Q. Song, P. Beggs, M. Easton, Compressive strain-rate sensitivity of magnesium-aluminum die casting alloys, Mater. Des. 30 (2009) 642–648.
[30] A.S. Khan, A. Pandey, T. Gnäupel-Herold, R.K. Mishra, Mechanical response and texture evolution of AZ31 alloy at large strains for different strain rates and temperatures, Int. J. Plast. 27 (2011) 688–706.
[31] R. Korla, A.H. Chokshi, Strain-rate sensitivity and microstructural evolution in a Mg-Al-Zn alloy, Scr. Mater. 63 (2010) 913–916.
[32] M.R. Barnett, A Taylor model based description of the proof stress of magnesium AZ31 during hot working, Metall. Mater. Trans. A 34 (2003) 1799–1806.
[33] M.R. Barnett, Twinning and the ductility of magnesium alloys: Part I: "Tension" twins, Mater. Sci. Eng. A 464 (2007) 1–7.
[34] H. Asgari, J.A. Szpunar, A.G. Odeshi, L.J. Zeng, E. Olsson, Effect of grain size on high strain rate deformation of rolled Mg-4Y-3RE alloy in compression, Mater. Sci. Eng. A 633 (2015) 92–102.
[35] H. Asgari, A.G. Odeshi, J.A. Szpunar, On dynamic deformation behavior of WE43 magnesium alloy sheet under shock loading conditions, Mater. Des. 63 (2014) 552–564.
[36] H. Asgari, A.G. Odeshi, J.A. Szpunar, L.J. Zeng, E. Olsson, D.Y. Li, Effect of yttrium on the twinning and plastic deformation of AE magnesium alloy under ballistic impact, Mater. Sci. Eng. A 623 (2015) 10–21.
[37] B. Li, S.P. Joshi, O. Almagri, Q. Ma, K.T. Ramesh, T. Mukai, Rate-dependent hardening due to twinning in an ultrafine-grained magnesium alloy, Acta Mater. 60 (2012) 1818–1826.
[38] M.A. Meyers, K.K. Chawla, Mechanical Behavior of Materials, Cambridge University Press, 2009.